Boosting oxygen reduction of single atomic iron sites by charge redistribution

Zhanli Han [a], Youqi Zhu [a],[*], Xiuyun Yao [a], Hui Peng [b], Changliang Du [a], Jiachen Tian [a], Lifen Yang [a], Xilan Ma [a], Jianhua Hou [c], Chuanbao Cao [a],[*]

[a] Research Center of Materials Science, Beijing Key Laboratory of Construction Tailorable Advanced Functional Materials and Green Applications, Beijing Institute of Technology, Beijing 100081, China
[b] Analysis and Testing Center, Shandong University of Technology, Zibo 255000, China
[c] School of Environmental Science and Engineering, Yangzhou University, Yangzhou 225000, China

ARTICLE INFO

ABSTRACT

Atomically dispersed porphyrin-type iron catalysts have demonstrated great potential to substitute platinum group metals for the oxygen reduction reaction (ORR), yet being subjected to limited active sites and sluggish O_2 activation kinetics over the symmetrical planar four-coordinated FeN_4 structure. Herein, the charge regulation on FeN_4 site is achieved via non-bonding interaction of adjacent nitrogen over high-loading single atomic Fe catalysts to boost their intrinsic ORR activity. The single atomic Fe catalysts exhibit excellent alkaline ORR activity with a half-wave potential of 0.914 V versus reversible hydrogen electrode and tenfold higher kinetic current density than that of Pt/C catalysts. Both experimental and theoretical studies confirm that the secondary nitrogen compensation can anchor greater Fe atoms up to 5.44 wt% with sufficient O_2 activation sites and simultaneously break the symmetrical charge distribution of FeN_4 site to optimize the adsorption/desorption of oxygen intermediate for accelerating ORR kinetics. Moreover, the single atomic Fe catalysts demonstrate great practical application in liquid and solid zinc-air batteries with long-term cycling stability for 600 and 150 h, respectively, as well as superior flexibility in solid batteries.

1. Introduction

The serious fossil energy crisis is intensively driving the evolution of sustainable key alternative technologies, such as fuel cells [1–3] and zinc-air batteries [4–6]. Nevertheless, the unsatisfactory ORR kinetics in air cathode has severely restricted their widespread applications [7–11]. Although Pt-based catalysts demonstrate high intrinsic ORR activity, they are defeated by exorbitant prices and poor long-term stability [12–15]. Tremendous endeavor has been made to explore alternatives to Pt-based catalysts [16–22]. Nitrogen-anchored single atomic Fe catalysts with symmetrical planar four-coordinated FeN_4 structure have demonstrated the most promising ORR activity [9,23–25]. Despite considerable achievements, boosting the overall ORR performances of single atomic Fe catalysts are urgently desired but challenging [26–30]. Crucial in achieving this objective is enhancing inherent activity of single FeN_4 site and endowing sufficient active-site availability [31–33]. It is therefore highly required to exploit reliable strategy for fabricating single atomic Fe catalysts with high-loading and superior intrinsic ORR

activity.

Single atomic Fe catalysts for ORR have been predominantly synthesized by pyrolysis method [24,34,35]. Unfortunately, the inevitable nitrogen loss during pyrolysis generally causes few nitrogen-coordinated trapping sites and thus low single-atom Fe loading [36]. Therefore, the extra nitrogen compensation is expected to be a promising route for achieving high-loading single atomic Fe catalysts [1,31]. Additionally, the local electronic structure engineering of FeN_4 site via regulating the coordination structure is extensively performed to modulate the desorption and adsorption energy of oxygen specie for improving their intrinsic activity [37–40]. Although the porphyrin-type FeN_4 sites demonstrate the most geometrically structural stability, the resultant symmetric electron distribution also severely obstructs the further improvement of ORR kinetics due to the unfavorable activation of oxygen intermediate [37,41–43]. Theoretically, breaking the symmetry of electron distribution of FeN_4 site can further accelerate ORR kinetics. Although incorporating extra coordination atoms (P, S, B etc.) with different electronegativity into the FeN_4 site to construct new

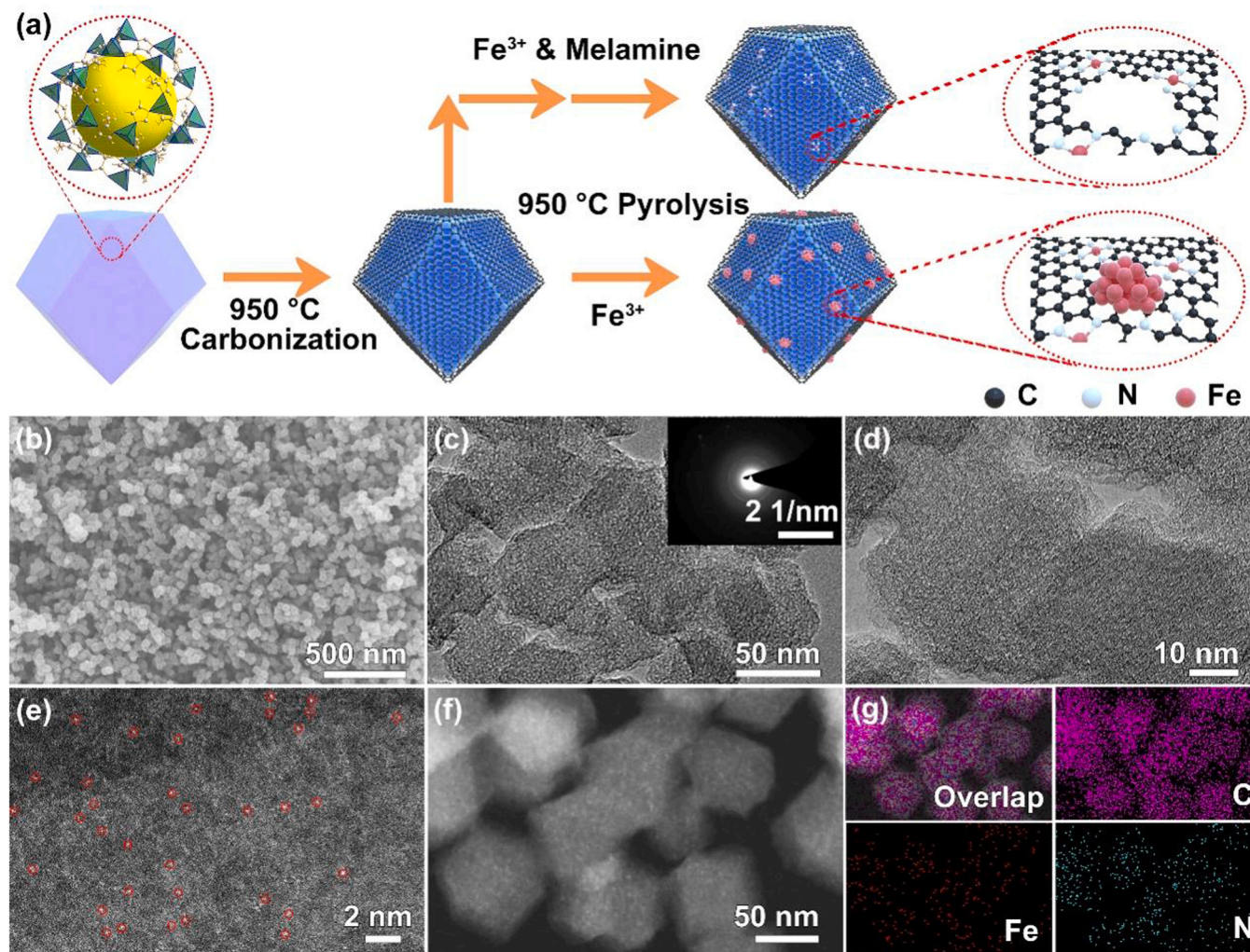**Fig. 1.** Synthesis and morphological characterization of Fe SACs/N-C. (a) Conventional diagram of preparation procedure. (b-c) SEM and TEM images with corresponding SAED pattern. (d-e) HR-TEM and AC HAADF-STEM images. (f) STEM image and (g) corresponding elemental mapping.

coordination structure is well developed, the highly nonequilibrium bonding interaction from the different coordination atoms could decrease the atomic structural stability of Fe active site [7,44–47]. Therefore, realizing asymmetrical electron distribution of FeN$_4$ site is highly desirable but still presents great obstacle.

Herein, a secondary nitrogen compensation strategy is proposed to fabricate high-loading single atomic Fe catalysts (denoted as Fe SACs/N-C) with enhanced intrinsic ORR activity. The external nitrogen can not only effectively trap and anchor more Fe atoms but also build nonbonding interaction by neighboring uncoordinated nitrogen to break the symmetrical charge distribution of FeN$_4$ site. Consequently, the Fe SACs/N-C presents high metal loading of 5.44 wt% and exhibits superior alkaline ORR performances with superb half-wave potential of 0.914 V versus reversible hydrogen electrode, which is 83 mV more positive than that of commercial Pt/C. The practical applications of Fe SACs/N-C catalysts are also evaluated in both liquid and solid zinc-air batteries, which can deliver unexceptionable stable lifespan over 600 and 150 h, respectively, as well as excellent flexibility in solid batteries. This work opens up unprecedented ideas for fabricating single atomic ORR catalysts with high loading and enhanced intrinsic activity.

2. Results and discussion

2.1. Structural and morphological characterization

The preparation process of Fe SACs/N-C is illustrated in Fig. 1a. The well-defined zeolitic imidazolate frameworks (ZIF-8) with particle size of 70 nm (Fig. S1 and S2) [2] were first pyrolyzed to produce porous nitrogen-doped carbon matrix (ZIF-8-NC, Fig. S3 and S4). Then, both Fe^{3+} ions and melamine molecules were absorbed on the porous carbon matrix in methanol solution under stirring. After pyrolysis under argon atmosphere, Fe SACs/N-C were prepared. The added melamine can serve as the extra nitrogen source to trap abundant Fe^{3+} ions at high temperature for achieving high-loading Fe single-atom catalysts. On the contrary, in absence of melamine, the high-temperature pyrolysis just produces ultrafine Fe nanoparticles embedded in the porous carbon matrix (Fe NPs/N-C) due to lack of sufficient coordination nitrogen atoms.

The scanning electron microscope (SEM) reveal that Fe SACs/N-C retain the initial polyhedral feature of the ZIF-8 and ZIF-8-NC precursors (Fig. 1b and Fig. S5). Both transmission electron microscopy (TEM) and high-resolution transmission electron microscopy (HR-TEM) images (Fig. 1c,d) demonstrate abundant micropores on the surface of Fe SACs/N-C, which are crucial to host Fe^{3+} ions during the absorption [48,49]. To explore the exact existence state of Fe species, the aberration-corrected high-angle annular dark-field scanning
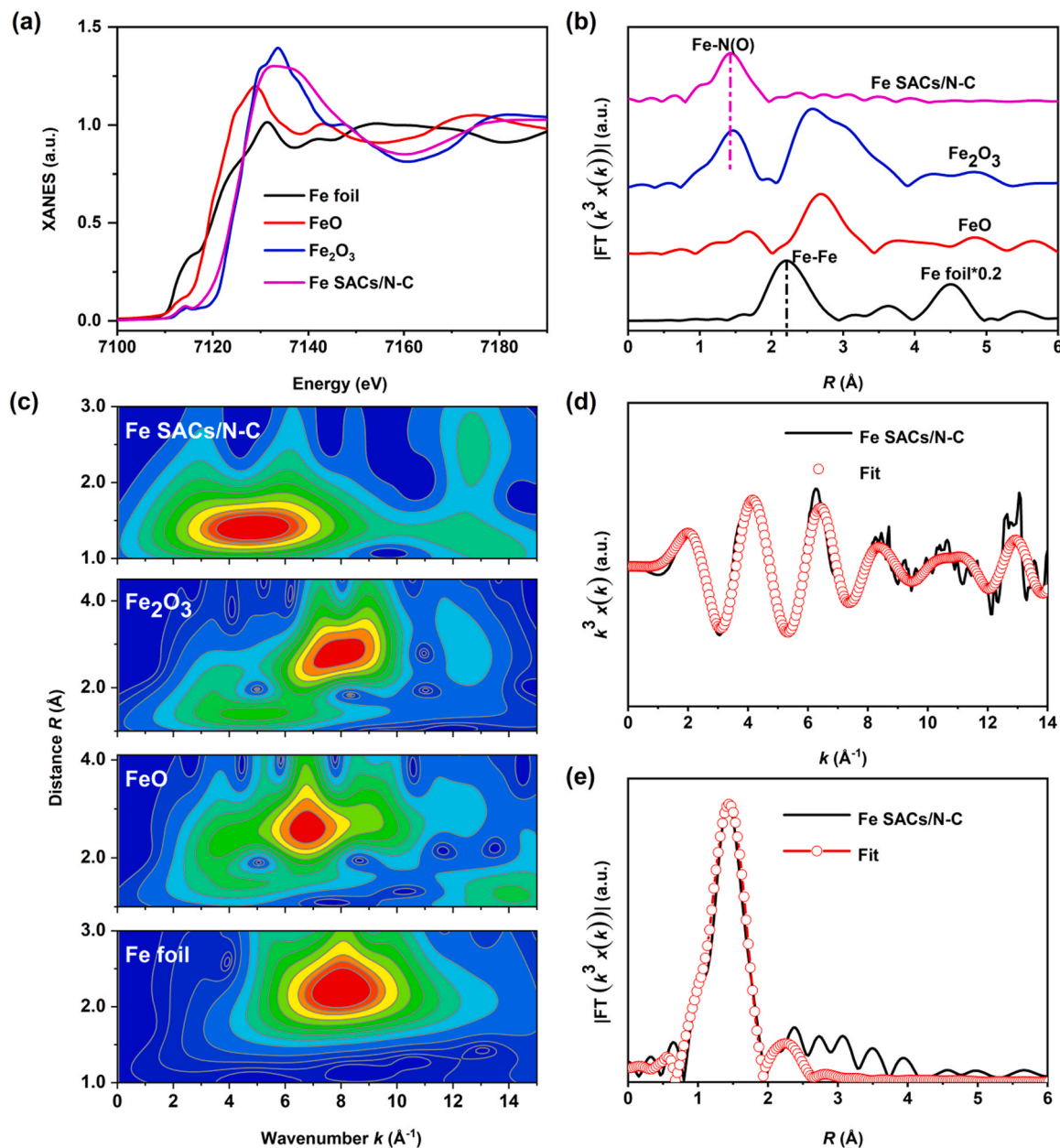
Fig. 2. X-ray absorption fine structure (XAFS) measurements of Fe SACs/N-C. (a) Fe K-edge XANES spectra. (b) Fourier transformed (FT) k^3-weighted χ (k)-function of the EXAFS spectra for Fe K-edge. (c) WT for the k^3-weighted EXAFS signals. (d) and (e) Corresponding FT-EXAFS fitting curves in k and R space, respectively.

transmission electron microscope (AC HAADF-STEM) was conducted. Abundant atomically dispersed light spots derived from Fe atoms could be distinctly discerned in nanocarbon matrix owing to the significant difference of Z-contrast between Fe and C as well N atoms (Fig. 1e) [50, 51]. Besides, no Fe particles or clusters are observed, which initially confirms the successful synthesis of single atomic Fe catalysts. STEM image (Fig. 1f) and relevant energy-dispersive X-ray (EDX) spectroscopy elemental mapping (Fig. 1g) show that the Fe, C and N elements are uniformly dispersed throughout the carbon material. By contrast, although Fe NPs/N-C exhibit analogous surface texture (Fig. S6a,b) to Fe SACs/N-C, the STEM images (Fig. S6d) verify the existence of massive Fe nanoparticles, which are further demonstrated by the observed lattice distance (2.04 Å) related to the (110) planes of metallic Fe nanoparticles (Fig. S6c) [52,53].

Fe SACs/N-C display a significantly larger Brunauer-Emmett-Teller (BET) surface area and smaller pore size in diameter with respect to Fe NPs/N-C (Fig. S7 and Table S1), which should be derived from the

absence of Fe particles. X-ray diffraction (XRD) patterns (Fig. S8) reveal a typical amorphous carbon configuration of Fe SACs/N-C without any other diffraction peaks of Fe-based crystalline phases [54]. By contrast, Fe NPs/N-C exhibit characteristic signals of metal Fe species [31,53]. Raman spectra (Fig. S9) present two predominant bands near 1350 (D peak) and 1580 (G peak) cm^{-1}, which are relevant to the defect-induced vibrations and the tangential stretch of sp^2-hybridized graphite framework domain [55]. The I_D/I_G values of Fe SACs/N-C, ZIF-8-NC and Fe NPs/N-C are 2.57, 2.63 and 1.82, suggesting the defect-rich carbon structure of these three catalysts. The obviously varied I_D/I_G value of Fe NPs/N-C in comparison to those of Fe SACs/N-C and ZIF-8-NC indicates that Fe nanoparticles encapsulation can improve the relative content of sp^2-hybridized carbon atoms [56], but single atomic Fe insertion has no effect on the structural feature of the carbon substrate.

X-ray photoelectron spectroscopy (XPS) was performed to reveal the working mechanism of the secondary nitrogen compensation on elemental composition and binding configuration of Fe SACs/N-C and Fe
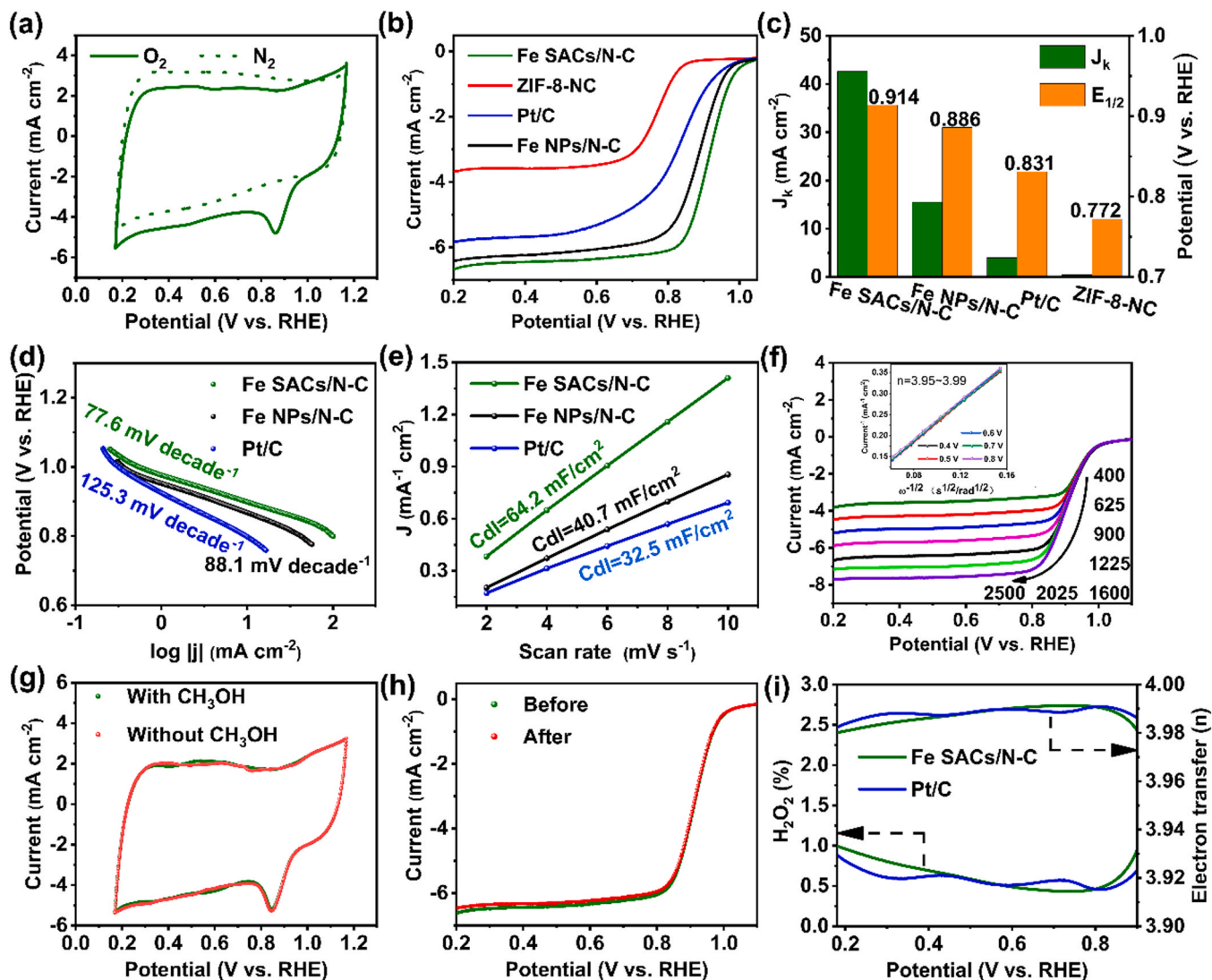
Fig. 3. ORR performance of Fe SACs/N-C catalysts. (a) CV curves in N_2- and O_2-saturated 0.1 M KOH electrolyte. (b) LSV plots at 1600 rpm rotation. (c) The bar graph of J_k and $E_{1/2}$. (d) Electrochemical double-layer capacitance (C_{dl}). (e) Tafel plots. (f) LSV plots at various rotating rates (inset showing the K-L plots). (g) CV curves without and with 1.0 M methanol. (h) LSV plots before and after 10,000 potential cycles. (i) The number of electron transfer (n) and H_2O_2 yield.

NPs/N-C. The full XPS spectra display the peaks originated from Fe, N, O and C of the two samples (Fig. S10). With the extra addition of melamine, the Fe and N contents of Fe SACs/N-C and Fe NPs/N-C increase from 2.76 wt% and 5.11–5.09 wt% and 10.52 wt% (Table S2). The observed Fe content for Fe SACs/N-C and Fe NPs/N-C are nearly equivalent to the precise value of 5.44 wt% and 2.93 wt% measured by inductively coupled plasma-atomic emission spectroscopy (ICP-AES). The high-resolution N 1 s spectra (Fig. S11) indicate the coexistence of four types of peaks corresponding to pyridinic N, Fe-N, graphitic N, and oxidized N, respectively [37]. In comparison with Fe NPs/N-C, Fe SACs/N-C exhibit a dramatically higher ratio of the pyridinic N content (Fig. S12), which ultimately determines the performance of the catalysts by restructuring the charge distribution of active sites. These results demonstrate that the secondary nitrogen compensation strategy can not only improve the nitrogen content in carbon substrate to fabricate abundant nitrogen-coordinated sites for trapping much more Fe atoms to prevent their aggregation into nanoparticles, but also engineer the electronic structure of active sites, so as to obtain the high-loading single-atom catalysts with boosted intrinsic activity.

Synchrotron X-ray absorption fine structure (XAFS) analyses were conducted to further uncover the coordination state and atomic structure of Fe species in Fe SACs/N-C [25,32,57]. Fig. 2a exhibits the

normalized X-ray absorption near edge structure (XANES) profiles of Fe K-edge for Fe SACs/N-C, Fe foil, Fe_2O_3 and FeO for comparison. Fe SACs/N-C show the relatively smooth spectroscopy shape without obvious oscillations. The absorption edge position of Fe SACs/N-C is very adjacent to that of Fe_2O_3 reference, suggesting that Fe species is more positively charged with an average oxidized state nearly identical to Fe^{3+} valence.

The standard pre-edge peak of Fe SACs/N-C is associated with the 1s-4pz transition and can serve as the fingerprint of a spatial four-coordinated structure. Fig. 2b demonstrates the Fourier transformed (FT) k^3-weighted extended X-ray absorption fine structure (EXAFS) spectra. Fe SACs/N-C show one prominent peak near 1.47 Å that can be ascribed to the backscattering pair between Fe and the coordinated light species. The Fe_2O_3 counterpart also displays one main peak of Fe-O coordination shells near 1.47 Å. Accordingly, the observed main peak of Fe SACs/N-C can be attributed to the Fe-N/C coordination shell. In comparison, Fe foil exhibits a main peak 2.2 Å that can be ascribed to the metallic Fe-Fe coordination shell. In addition, the Fe-Fe coordination peak of Fe SACs/N-C is nearly neglectful and no other high-shell peaks are observed, which demonstrates that the Fe-containing species is atomically dispersed.

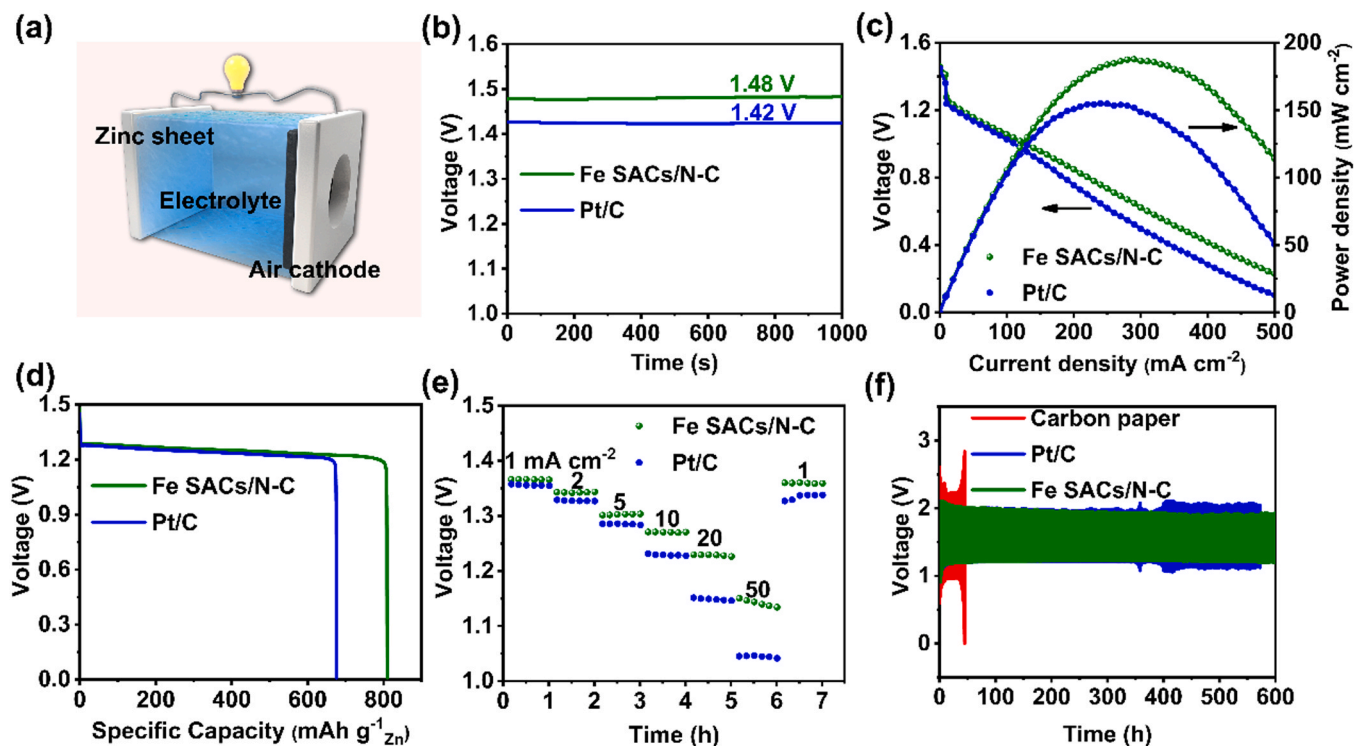The wavelet transform (WT) of Fe K-edge EXAFS oscillation is a

Fig. 4. The electrochemical performance of Fe SACs/N-C air cathode in liquid zinc-air batteries. (a) Structural illustration of the home-made battery. (b) The OCV curves. (c) Discharge polarization plots and relevant power density profiles at 10 mA cm^{-2}. (d) Specific capacity plots at 10 mA cm^{-2}. (e) Different current densities discharge plots. (f) Galvanostatic long-term charge and discharge profiles at 5.0 mA cm^{-2}.

powerful and informative technique to extract the 2D-representation of linear spectrum signal for uncovering high-resolution information in both k and R spaces simultaneously. The WT contour plots (Fig. 2c) of Fe SACs/N-C exhibit only one peak near 4.7 Å assigned to the Fe-N/C co-ordination and no peak originated from Fe-Fe coordination (7.8 Å) is present. These investigations further manifest that Fe species in Fe SACs/N-C are dispersed as single atomic sites. The precise coordination configurations of Fe atoms were investigated by quantitative EXAFS curve fitting (Fig. 2d,e). The well-fitting analysis definitely shows that the main peak near 1.47 Å could be well interpreted as the first Fe-N coordination shell of the porphyrin-type FeN_4 moieties in the Fe SASs/N-C. The coordination number (4.0) and other structural parameters of center Fe atom of Fe SACs/N-C are listed in Table S3.

2.2. Electrocatalytic performance

The alkaline ORR catalytic properties of Fe SACs/N-C were assessed by various electrochemical measurements in 0.1 M KOH medium by the rotating disk electrode (RDE). Cyclic voltammograms (CV) plots were conducted in N_2- and O_2-saturated medium at a scanning speed of 50 mV s^{-1}, respectively. An obvious cathode peak is appeared in O_2-saturated electrolyte but absent in N_2-saturated condition, indicative of an evident oxygen reduction process in the Fe SACs/N-C (Fig. 3a) [56]. Simultaneously, the Fe NPs/N-C and commercial 20 % Pt/C exhibit the similar CV shape to that of Fe SACs/N-C in both N_2- and O_2-saturated electrolyte but with more negative cathodic peak potential (Fig. S13), indicating that the Fe SACs/N-C catalysts can deliver better catalytic activity for ORR. To further explore the catalytic activity of Fe SACs/N-C, the liner sweep voltammograms (LSV) were measured using RDE technique at a rotation of 1600 rpm. As shown in Fig. 3b, the Fe SACs/N-C show the highest half-wave potential ($E_{1/2}$) of 0.914 V_{RHE} (versus reversible hydrogen electrode), which is far superior to that of Pt/C (0.831 V_{RHE}) and the most Fe-based ORR electrocatalysts reported to date (Table S4). In addition, the fresh ZIF-8-NC exhibits a $E_{1/2}$ of

0.772 V_{RHE}, which is much lower than that of Fe SACs/N-C catalysts, demonstrating that the FeN_4 sites play the key role in ORR performance. Importantly, Fe SACs/N-C also exhibit better $E_{1/2}$ than that (0.886 V_{RHE}) of Fe NPs/N-C, which can be ascribed to high-loading FeN_4 catalytic active sites with boosted intrinsic activity. Besides, the Fe SACs/N-C display the optimal kinetic current density (J_k) of 42.6 mA cm^{-2} at 0.85 V_{RHE}, which is tenfold higher than that of Pt/C (Fig. 3c).

The Tafel slope (Fig. 3d) of Fe SACs/N-C is calculated to be 77.6 mV dec^{-1}, while 88.1 and 125.3 mV dec^{-1} for Fe NPs/N-C and Pt/C, respectively. The superior J_k and Tafel slope reveal the faster kinetics for Fe SACs/N-C catalysts [34]. The corresponding mass activity (MA) and turnover frequency (TOF) of Fe SACs/N-C are 16403.9 A g_{Fe}^{-1} and 9.49 s^{-1}, respectively, outperforming those of Pt/C (39.2 A g_{Pt}^{-1} and 0.08 s^{-1}). Furthermore, Fe SACs/N-C present much higher C_{dl} value (64.2 mF cm^{-2}) than that of Fe NPs/N-C (40.7 mF cm^{-2}) and Pt/C (32.5 mF cm^{-2}), indicating the secondary nitrogen compensation can facilitate the improvement in electrochemically active surface area (ESCA) as shown in Fig. 3e and Fig. S14).

To reveal the ORR mechanism of Fe SACs/N-C catalysts, LSV plots at various rotating rates from 400 to 2500 rpm were performed. The limiting current densities exhibit an obvious enhancement with the gradually elevated rotation rates, while the onset potential maintains constant, indicative of the oxygen diffusion-limiting ORR current (Fig. 3f). The relevant Koutecky-Levich (K-L) plots are nearly linear, suggesting the first-order reaction kinetics during the ORR process [5]. The electron-transfer number (n) is ranging from 3.95 to 3.99, indicating an effective four-electron ORR process for Fe SACs/N-C catalysts. By contrast, the n is ranging from 3.91 to 3.97 and from 3.82 to 3.89 for Fe NPs/N-C and Pt/C, respectively (Fig. S15). The CV curves in O_2-saturated 0.1 M KOH electrolyte with and without 1.0 M methanol were collected to evaluate the methanol resistance of Fe SACs/N-C and Fe NPs/N-C catalysts. As shown in Fig. 3g and Fig. S16, both the two catalysts show nearly overlapped CV curves even after methanol injection, indicative of the outstanding methanol resistance [4]. The LSV long
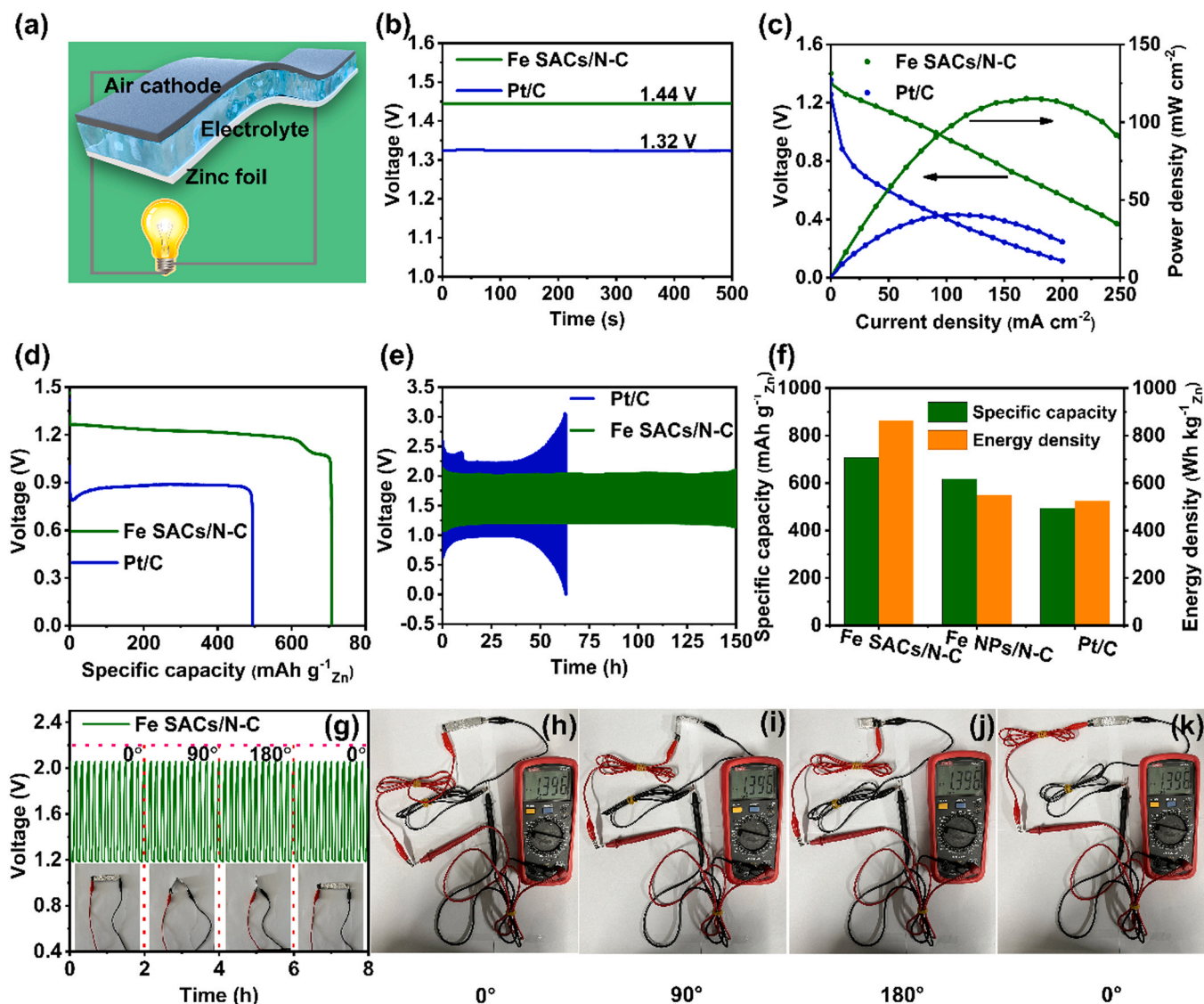
Fig. 5. The performances of the Fe SACs/N-C air cathode in solid zinc-air batteries. (a) Structural illustration. (b) The OCV curves. (c) Discharge polarization plots and relevant power density profiles at 10 mA cm^{-2}. (d) Specific capacity plots at 10 mA cm^{-2}. (e) Galvanostatic long-term charge and discharge profiles at 5.0 mA cm^{-2}. (f) Specific capacity and energy density. (g-k) Galvanostatic long-term charge and discharge profiles and open-circuit voltages under different bending angles.

cycle test was used to investigate the stability of catalysts. The voltage range and scan rate of the CV cycle between two LSV tests are 0.2–1.2 V and 50 mV s^{-1} respectively. For Fe SACs/N-C catalysts, the $E_{1/2}$ and limiting current density are almost unchanged even after repetitive 10, 000 cycles, indicating the excellent stability (Fig. 3h). For comparison, both Fe NPs/N-C and Pt/C show significant attenuation after long cycle (Fig. S17). Furthermore, the rotating ring disk electrode (RRDE) test results demonstrate the lowest H$_2$O$_2$ yield in the potential range 0.2–0.9 V$_{RHE}$ and the maximum n of 3.98–3.99 for Fe SACs/N-C (Fig. 3i and Fig. S18), indicating that the Fe SACs/N-C undergo an efficient catalytic process via a four-electron ORR process.

2.3. The performance of liquid zinc-air batteries

The Fe SACs/N-C were further employed as air cathode materials for liquid and solid zinc-air batteries for evaluating their potential application. Fig. 4a shows the structural model of the liquid zinc-air battery. The open-circuit voltage (OCV) of Fe SACs/N-C is 1.48 V, surpassing that of Pt/C (1.42 V) and Fe NPs/N-C (1.46 V) as shown in Fig. 4b and Fig. S19. Furthermore, light-emitting diode (LED) panel display and

lamp could be successfully powered by one device and two in series, respectively (Fig. S20). Besides, Fe SACs/N-C show excellent peak power density (187.8 mW cm^{-2}) and specific capacity (850.0 mAh g$_{Zn}^{-1}$), higher than that of Pt/C and Fe NPs/N-C (Fig. 4c,d and Fig. S21-S22). Besides, the Fe SACs/N-C show the least decline of discharge voltage at various current densities, indicative of much better rate capability (Fig. 4e and Fig. S23). The long-term cyclability curves were performed at a current density of 5.0 mA cm^{-2} with each cycle being 20 min and shown in Fig. 4f and Fig. S24. Compared with hydrophobic carbon paper, Pt/C and Fe NPs/N-C, Fe SACs/N-C exhibit a much narrower voltage gap of 0.72 V (1.22 and 1.94 V for discharge and charge, respectively), achieving the high energy efficiency of 62.9 %. Notably, Fe SACs/N-C demonstrate an excellent long-term cycling durability over 600 h without significant voltage drop, which are superior to the most reported catalysts for liquid zinc-air batteries (Table S5).

2.4. The performance of solid zinc-air batteries

Inspired by the outstanding performance of Fe SACs/N-C air cathode in liquid zinc-air batteries, the solid zinc-air batteries were fabricated
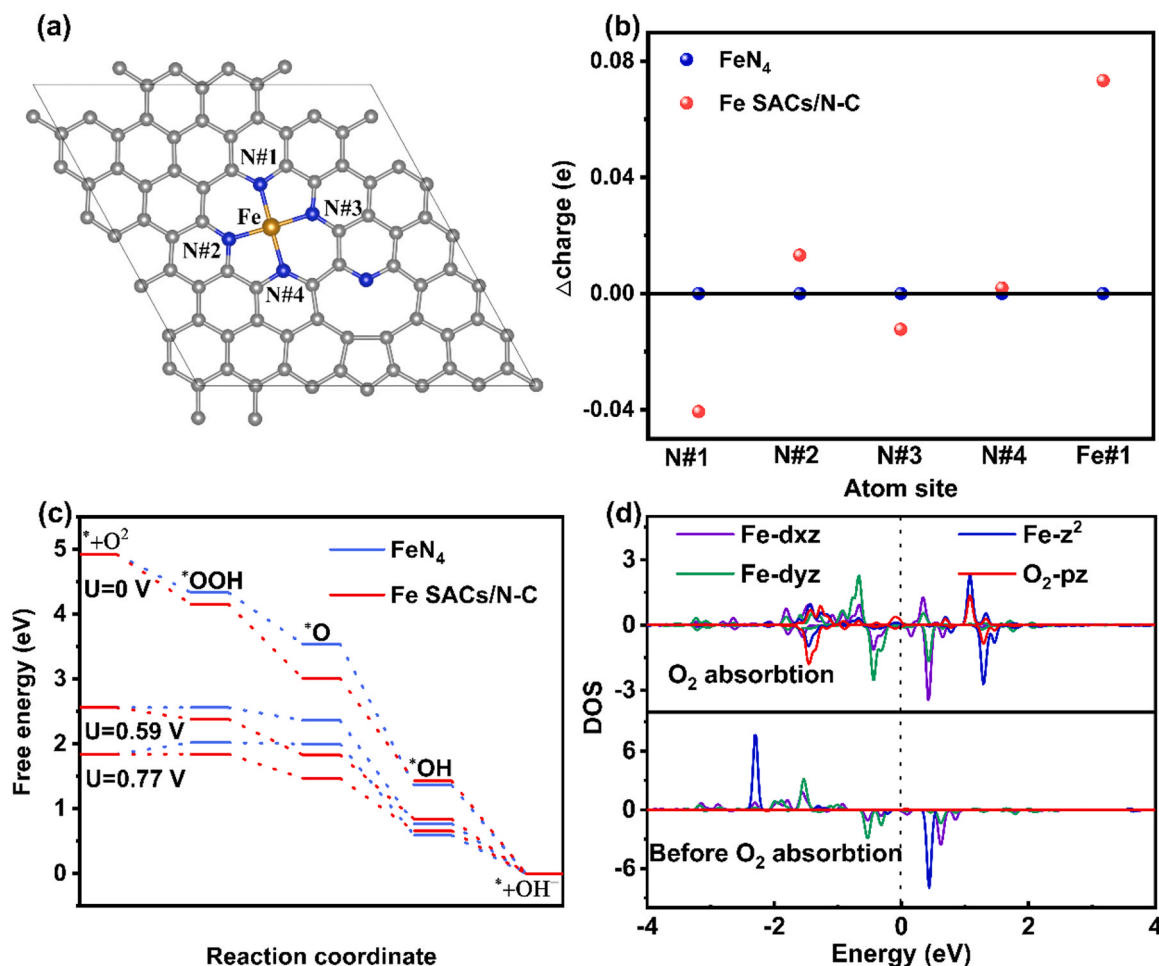
Fig. 6. Theoretical calculations and ORR mechanism. (a) Optimized configuration. (b) Relative charge of the first coordination layer. (c) Free energy diagrams. (d) DOS plots of O_2 activation.

(Fig. 5a). The OCV of the solid batteries with Fe SACs/N-C air cathode is up to 1.44 V, much larger than that of Fe NPs/N-C and Pt/C (Fig. 5b and Fig. S25). Notably, the batteries for Fe SACs/N-C not only light the LED panel display and lamp by one device and two in series, respectively, but also the former is not affected when the battery is randomly bent to different angles of 0°, 90°, and 180° (Fig. S26 and Video 1), which indicates that the solid zinc-air battery possesses excellent flexibility and stable operation. Moreover, the batteries exhibit superior specific capacity of 707.9 mAh g_{Zn}^{-1} and outstanding peak power density of 115.1 mW cm^{-2} (Fig. 5c,d,f and Fig. S27), which surpass the most reported solid zinc-air batteries (Table S6). The long-term cyclability curves were performed at a current density of 5.0 mA cm^{-2} with each cycle being 10 min. The batteries with Fe SACs/N-C air cathode demonstrate no significant voltage decay over 150 h galvanostatic discharge-charge cycles, whereas the batteries with Fe NPs/N-C and Pt/ C air cathode show limited cycle life (Fig. 5e, Fig. S28). Galvanostatic discharge-charge cycling curves and the OCV under different bending angles for Fe SACs/N-C air cathode were conducted to further explore the flexibility of solid zinc-air batteries. Fig. 5g- k reveal almost consistent potential plateaus and open-circuit voltages under different bending conditions, which once again display the remarkable flexibility of the solid zinc-air batteries. Undoubtedly, the breathtaking batteries performances should be attributed to high single-atom loading and boosted intrinsic activity of the Fe SACs/N-C.

Supplementary material related to this article can be found online at doi:10.1016/j.apcatb.2023.122961.

2.5. Density functional theory (DFT) calculation

Density functional theory (DFT) calculation was preformed to reveal the ORR mechanism and the origin of the superior catalytic activity and stability of Fe SACs/N-C [37,46,58]. Based on the electrochemical and characterization results, two types of structure models were constructed, namely the standard planar symmetrical four-coordinated FeN$_4$ center embedded in graphene matrix (denoted as FeN$_4$) and the charge-redistributing FeN$_4$ site with neighboring uncoordinated pyridinic nitrogen doping at different positions (denoted as Fe SACs/N-C, 2, 3, 4, and 5, Fig. 6a and Fig. S29-S34). All the computational details are based on the proposed four-electron ORR process in alkaline electrolyte as listed in Fig. S35. As shown in Fig. 6b, the Bader charge analysis shows that the symmetric charge distribution of the Fe-N$_4$ sites is broken by coupling with extra neighboring uncoordinated pyridinic nitrogen. The Fe SACs/N-C deliver a more positive charge state in Fe sites than that in standard FeN$_4$ structure, which is attributed to the strong electron capture capability of pyridinic nitrogen.

Fig. 6c exhibits the free-energy pathways of the four-electron ORR process on FeN$_4$ and Fe SACs/N-C in alkaline electrolyte at different electrode potential (U). It is definite that the rate-determining step (RDS) of ORR process on both FeN$_4$ and Fe SACs/N-C is the conversion of O_2 into OOH* by the free energy calculations. At U= 0 V, all the reaction steps from O_2 to OH$^-$ are downhill, implying a spontaneous process. At U= 0.59 V, for FeN$_4$, the subtraction step from O_2 to OOH* takes place, while the other subtractions remain downhill, suggesting that the limiting potential for FeN$_4$ is 0.59 V. For the Fe SACs/N-C, all reaction

steps are exothermic process base on the fact that all of subtractions are downhill. Similarly, it is obvious that the limiting potential for Fe SACs/ N-C is 0.77 V by analyzing the subtraction step at U= 0.77 V, while the conversion of O_2 into OOH* is endothermic process for FeN_4. Besides, the limiting potentials for Fe SACs/N-C-2, 3, 4, and 5 are 0.67, 0.64, 0.64, and 0.71 V, respectively (Fig. S36), which all surpass that of FeN_4. Therefore, the charge-redistributing FeN_4 centers with neighboring uncoordinated pyridinic nitrogen doping possess much better theoretical ORR activity and smaller overpotential compared with the standard FeN_4, which is well consistent with the above experimental results. To further reveal the nature of O_2 activation and the electron structure of the single-atom Fe center, the density of states (DOS) of O_2 and FeN_4 center with and without pyridine nitrogen doping at different positions were performed. As a representative of FeN_4 center with nitrogen doping, the DOS of Fe SACs/N-C is shown in Fig. 6d. Before O_2 is adsorbed on the Fe site, the electrons are mainly accumulated on the dz^2 orbital of Fe. After absorbing O_2, the *d* orbital of Fe interacts with the *pz* orbital of O_2 to form hybrid states and the electrons of Fe SACs/N-C transfer from Fe dz^2 to the O_2 *pz* orbital. Compared with FeN_4 (Fig. S37), more electrons are accommodated into the conjugated molecular orbitals for Fe SACs/N-C and other FeN_4 structure with pyridine nitrogen doping at different positions (Fig. S38–41), which increases substantially the adsorption energies of oxygen-containing species and boosts the ORR intrinsic catalytic activity.

3. Conclusions

In summary, Fe SACs/N-C catalysts with high-loading Fe single-atom (5.44 wt%) are successfully synthesized by novel secondary nitrogen supplementation strategy. Benefiting from the dense catalytic active sites with boosted intrinsic activity, Fe SACs/N-C exhibit excellent alkaline ORR electrocatalytic activity and stability. As expected, the homemade liquid and solid zinc-air batteries deliver outstanding practical application ability, and superior flexibility in solid batteries as well. DFT calculations reveal that the introduced external nitrogen sources effectively regulate the charge distribution of the catalytic active center, which increases adsorption energies of oxygen-containing species, thus accelerating the ORR kinetic process. This study provides a brilliant strategy to develop ORR electrocatalysts with ultrahigh single atomic loads and boosted intrinsic activity and facilitate the commercial application of liquid and flexible solid zinc-air batteries.

CRediT authorship contribution statement

Zhanli Han: Conception and design, Experiment, Data analysis, Writing – original draft. **Youqi Zhu:** Supervision, Writing – review & editing. **Xiuyun Yao:** Electrochemistry testing. **Hui Peng:** Synchrotron radiation testing. **Changliang Du:** XRD testing. **Jiachen Tian:** TEM testing. **Lifen Yang:** SEM testing. **Xilan Ma:** Supervision. **Jianhua Hou:** Supervision. **Chuanbao Cao:** Supervision, Writing – review & editing, Funding acquisition.

Declaration of Competing Interest

The authors declare that they have no known competing financial interests or personal relationships that could have appeared to influence the work reported in this paper.

Data availability

The data shared in Supporting Information.

Acknowledgements

Appendix A. Supporting information

Supplementary data associated with this article can be found in the online version at doi:10.1016/j.apcatb.2023.122961.

References

[1] J. Li, M. Chen, D.A. Cullen, S. Hwang, M. Wang, B. Li, K. Liu, S. Karakalos, M. Lucero, H. Zhang, C. Lei, H. Xu, G.E. Sterbinsky, Z. Feng, D. Su, K.L. More, G. Wang, Z. Wang, G. Wu, Atomically dispersed manganese catalysts for oxygen reduction in proton-exchange membrane fuel cells, Nat. Catal. 1 (12) (2018) 935–945, https://doi.org/10.1038/s41929-018-0164-8.

[2] L. Jiao, J. Li, L.L. Richard, Q. Sun, T. Stracensky, E. Liu, M.T. Sougrati, Z. Zhao, F. Yang, S. Zhong, H. Xu, S. Mukerjee, Y. Huang, D.A. Cullen, J.H. Park, M. Ferrandon, D.J. Myers, F. Jaouen, Q. Jia, Chemical vapour deposition of Fe-N-C oxygen reduction catalysts with full utilization of dense Fe-N4 sites, Nat. Mater. 20 (10) (2021) 1385–1391, https://doi.org/10.1038/s41563-021-01030-2.

[3] Y. Li, H.S. Pillai, T. Wang, S. Hwang, Y. Zhao, Z. Qiao, Q. Mu, S. Karakalos, M. Chen, J. Yang, D. Su, H. Xin, Y. Yan, G. Wu, High-performance ammonia oxidation catalysts for anion-exchange membrane direct ammonia fuel cells, Energy Environ. Sci. 14 (3) (2021) 1449–1460, https://doi.org/10.1039/d0ee03351k.

[4] Y. Chen, S. Ji, S. Zhao, W. Chen, J. Dong, W.C. Cheong, R. Shen, X. Wen, L. Zheng, A.I. Rykov, S. Cai, H. Tang, Z. Zhuang, C. Chen, Q. Peng, D. Wang, Y. Li, Enhanced oxygen reduction with single-atomic-site iron catalysts for a zinc-air battery and hydrogen-air fuel cell, Nat. Commun. 9 (1) (2018) 5422, https://doi.org/10.1038/s41467-018-07850-2.

[5] J. Balamurugan, T.T. Nguyen, N.H. Kim, D.H. Kim, J.H. Lee, Novel core-shell CuMo-oxynitride@N-doped graphene nanohybrid as multifunctional catalysts for rechargeable zinc-air batteries and water splitting, Nano Energy 85 (2021), 105987, https://doi.org/10.1016/j.nanoen.2021.105987.

[6] F. Lu, K. Fan, L. Cui, Y. Yang, W. Wang, G. Zhang, C. Wang, Q. Zhang, B. Li, L. Zong, L. Wang, Cu-N4 single atoms derived from metal-organic frameworks with trapped nitrogen-rich molecules and their use as efficient electrocatalysts for oxygen reduction reaction, Chem. Eng. J. 431 (2022), 133242, https://doi.org/10.1016/j.cej.2021.133242.

[7] K. Yuan, D. Lutzenkirchen-Hecht, L.B. Li, L. Shuai, Y.Z. Li, R. Cao, M. Qiu, X. D. Zhuang, M.H. Leung, Y.W. Chen, Boosting oxygen reduction of single iron active sites via geometric and electronic engineering: nitrogen and phosphorus dual-coordination, J. Am. Chem. Soc. 142 (5) (2020) 2404–2412, https://doi.org/10.1021/jacs.9b11852.

[8] B. Ji, J. Gou, Y. Zheng, X. Zhou, P. Kidkhunthod, Y. Wang, Q. Tang, Y. Tang, Metalloid-cluster ligands enabling stable and active FeN(4)-Te(n) motifs for the oxygen reduction reaction, Adv. Mater. 34 (28) (2022), e2202714, https://doi.org/10.1002/adma.202202714.

[9] C.X. Zhao, B.Q. Li, J.N. Liu, Q. Zhang, Intrinsic electrocatalytic activity regulation of M-N-C single-atom catalysts for oxygen reduction reaction, Angew. Chem. 60 (9) (2020) 4448–4463, https://doi.org/10.1002/anie.202003917.

[10] Z. Lin, A. Yang, B. Zhang, B. Liu, J. Zhu, Y. Tang, X. Qiu, Coupling the atomically dispersed Fe-N3 sites with sub-5 nm Pd nanocrystals confined in N-doped carbon nanobelts to boost the oxygen reduction for microbial fuel cells, Adv. Funct. Mater. 32 (5) (2021), 2107683, https://doi.org/10.1002/adfm.202107683.

[11] Y. Zhu, W. Sun, W. Chen, T. Cao, Y. Xiong, J. Luo, J. Dong, L. Zheng, J. Zhang, X. Wang, C. Chen, Q. Peng, D. Wang, Y. Li, Scale-up biomass pathway to cobalt single-site catalysts anchored on N-doped porous carbon nanobelt with ultrahigh surface area, Adv. Funct. Mater. 28 (37) (2018), 1802167, https://doi.org/10.1002/adfm.201802167.

[12] W.H. Lai, L. Zhang, Z. Yan, W. Hua, S. Indris, Y. Lei, H. Liu, Y.X. Wang, Z. Hu, H. K. Liu, S. Chou, G. Wang, S.X. Dou, Activating inert surface Pt single atoms via subsurface doping for oxygen reduction reaction, Nano Lett. 21 (19) (2021) 7970–7978, https://doi.org/10.1021/acs.nanolett.1c02013.

[13] Z. Qiao, C. Wang, C. Li, Y. Zeng, S. Hwang, B. Li, S. Karakalos, J. Park, A.J. Kropf, E.C. Wegener, Q. Gong, H. Xu, G. Wang, D.J. Myers, J. Xie, J.S. Spendelow, G. Wu, Atomically dispersed single iron sites for promoting Pt and Pt3Co fuel cell catalysts: performance and durability improvements, Energy Environ. Sci. 14 (9) (2021) 4948–4960, https://doi.org/10.1039/d1ee01675j.

[14] Y. Zhu, T. Cao, C. Cao, J. Luo, W. Chen, L. Zheng, J. Dong, J. Zhang, Y. Han, Z. Li, C. Chen, Q. Peng, D. Wang, Y. Li, One-pot pyrolysis to N-doped graphene with high-density Pt single atomic sites as heterogeneous catalyst for alkene hydrosilylation, ACS Catal. 8 (11) (2018) 10004–10011, https://doi.org/10.1021/acscatal.8b02624.

[15] Z. Yang, M. Xiang, M. Zhu, J. Hui, Y. Jiang, S. Dong, C. Yu, J. Ou, H. Qin, Single-atom platinum or ruthenium on C4N as 2D high-performance electrocatalysts for oxygen reduction reaction, Chem. Eng. J. 426 (2021) 131347, https://doi.org/10.1016/j.cej.2021.131347.

[16] D. Yu, Y. Ma, F. Hu, C.C. Lin, L. Li, H.Y. Chen, X. Han, S. Peng, Dual-sites coordination engineering of single atom catalysts for flexible metal-air batteries, Adv. Energy Mater. 11 (30) (2021), 2101242, https://doi.org/10.1002/aenm.202101242.

[17] W. Fan, Z. Duan, W. Liu, R. Mehmood, J. Qu, Y. Cao, X. Guo, J. Zhong, F. Zhang, Rational design of heterogenized molecular phthalocyanine hybrid single-atom

electrocatalyst towards two-electron oxygen reduction, Nat. Commun. 14 (1) (2023) 1426, https://doi.org/10.1038/s41467-023-37066-y.

[18] C. Gao, F. Lyu, Y. Yin, Encapsulated metal nanoparticles for catalysis, Chem. Rev. 121 (2) (2020) 834–881, https://doi.org/10.1021/acs.chemrev.0c00237.

[19] M.A. Ahsan, A.R. Puente Santiago, Y. Hong, N. Zhang, M. Cano, E. Rodriguez-Castellon, L. Echegoyen, S.T. Sreenivasan, J.C. Noveron, Tuning of trifunctional NiCu bimetallic nanoparticles confined in a porous carbon network with surface composition and local structural distortions for the electrocatalytic oxygen reduction, oxygen and hydrogen evolution reactions, J. Am. Chem. Soc. 142 (34) (2020) 14688–14701, https://doi.org/10.1021/jacs.0c06960.

[20] D. Deng, J. Qian, X. Liu, H. Li, D. Su, H. Li, H. Li, L. Xu, Non-covalent interaction of atomically dispersed Cu and Zn pair sites for efficient oxygen reduction reaction, Adv. Funct. Mater. 32 (32) (2022), 2203471, https://doi.org/10.1002/adfm.202203471.

[21] S. Wu, D. Deng, E. Zhang, H. Li, L. Xu, CoN nanoparticles anchored on ultra-thin N-doped graphene as the oxygen reduction electrocatalyst for highly stable zinc-air batteries, Carbon 196 (2022) 347–353, https://doi.org/10.1016/j.carbon.2022.04.043.

[22] X. Yao, Y. Zhu, T. Xia, Z. Han, C. Du, L. Yang, J. Tian, X. Ma, J. Hou, C. Cao, Tuning carbon defect in copper single-atom catalysts for efficient oxygen reduction, Small (2023), e2301075, https://doi.org/10.1002/smll.202301075.

[23] Y. Peng, B. Lu, S. Chen, Carbon-supported single atom catalysts for electrochemical energy conversion and storage, Adv. Mater. 30 (48) (2018), e1801995, https://doi.org/10.1002/adma.201801995.

[24] S.H. Yin, S.L. Yang, G. Li, G. Li, B.W. Zhang, C.T. Wang, M.S. Chen, H.G. Liao, J. Yang, Y.X. Jiang, S.G. Sun, Seizing gaseous Fe2+ to densify O2-accessible Fe–N_4 sites for high-performance proton exchange membrane fuel cells, Energ. Environ. Sci. 15 (7) (2022) 3033–3040, https://doi.org/10.1039/d2ee00061j.

[25] J. Tian, Y. Zhu, X. Yao, L. Yang, C. Du, Z. Lv, M. Hou, S. Zhang, X. Ma, C. Cao, Chemical vapor deposition towards atomically dispersed iron catalysts for efficient oxygen reduction, J. Mater. Chem. A 11 (10) (2023) 5288–5295, https://doi.org/10.1039/d2ta08943b.

[26] Y. Wang, H. Su, Y. He, L. Li, S. Zhu, H. Shen, P. Xie, X. Fu, G. Zhou, C. Feng, D. Zhao, F. Xiao, X. Zhu, Y. Zeng, M. Shao, S. Chen, G. Wu, J. Zeng, C. Wang, Advanced electrocatalysts with single-metal-atom active sites, Chem. Rev. 120 (21) (2020) 12217–12314, https://doi.org/10.1021/acs.chemrev.0c00594.

[27] Y. Chen, R. Gao, S. Ji, H. Li, K. Tang, P. Jiang, H. Hu, Z. Zhang, H. Hao, Q. Qu, X. Liang, W. Chen, J. Dong, D. Wang, Y. Li, Atomic-level modulation of electronic density of metal-organic frameworks-derived Co single-atom sites to enhance oxygen reduction performance, Angew. Chem. 60 (6) (2021) 3212–3221, https://doi.org/10.1002/anie.202012798.

[28] X. Zhao, X. Li, Z. Bi, Y. Wang, H. Zhang, X. Zhou, Q. Wang, Y. Zhou, H. Wang, G. Hu, Boron modulating electronic structure of FeN4C to initiate high-efficiency oxygen reduction reaction and high-performance zinc-air battery, J. Energy Chem. 66 (2022) 514–524, https://doi.org/10.1016/j.jechem.2021.08.067.

[29] X. Yao, Y. Zhu, Z. Han, L. Yang, J. Tian, T. Xia, H. Peng, C. Cao, Solvent-mediated oxidative polymerization to atomically dispersed iron sites for oxygen reduction, Appl. Catal. B: Environ. 331 (2023), 122675, https://doi.org/10.1016/j.apcatb.2023.122675.

[30] L. Xu, S. Wu, X. He, H. Wang, D. Deng, J. Wu, H. Li, Interface engineering of anti-perovskite Ni3FeN/VN heterostructure for high-performance rechargeable zinc-air batteries, Chem. Eng. J. 437 (2022), 135291, https://doi.org/10.1016/j.cej.2022.135291.

[31] L. Zhao, Y. Zhang, L.B. Huang, X.Z. Liu, Q.H. Zhang, C. He, Z.Y. Wu, L.J. Zhang, J. Wu, W. Yang, L. Gu, J.S. Hu, L.J. Wan, Cascade anchoring strategy for general mass production of high-loading single-atomic metal-nitrogen catalysts, Nat. Commun. 10 (1) (2019) 1278, https://doi.org/10.1038/s41467-019-09290-y.

[32] Q. Li, W. Chen, H. Xiao, Y. Gong, Z. Li, L. Zheng, X. Zheng, W. Yan, W.C. Cheong, R. Shen, N. Fu, L. Gu, Z. Zhuang, C. Chen, D. Wang, Q. Peng, J. Li, Y. Li, Fe isolated single atoms on S, N codoped carbon by copolymer pyrolysis strategy for highly efficient oxygen reduction reaction, Adv. Mater. 30 (25) (2018), e1800588, https://doi.org/10.1002/adma.201800588.

[33] Y. Xiong, W. Sun, P. Xin, W. Chen, X. Zheng, W. Yan, L. Zheng, J. Dong, J. Zhang, D. Wang, Y. Li, Gram-scale synthesis of high-loading single-atomic-site Fe catalysts for effective epoxidation of styrene, Adv. Mater. 32 (34) (2020), e2000896, https://doi.org/10.1002/adma.202000896.

[34] J. Han, H. Bao, J.Q. Wang, L. Zheng, S. Sun, Z.L. Wang, C. Sun, 3D N-doped ordered mesoporous carbon supported single-atom Fe-N-C catalysts with superior performance for oxygen reduction reaction and zinc-air battery, Appl. Catal. B: Environ. 280 (2021) 119411, https://doi.org/10.1016/j.apcatb.2020.119411.

[35] L. Zhong, C. Jiang, M. Zheng, X. Peng, T. Liu, S. Xi, X. Chi, Q. Zhang, L. Gu, S. Zhang, G. Shi, L. Zhang, K. Wu, Z. Chen, T. Li, M. Dahbi, J. Alami, K. Amine, J. Lu, Wood carbon based single-atom catalyst for rechargeable Zn-Air batteries, ACS Energy Lett. 6 (10) (2021) 3624–3633, https://doi.org/10.1021/acsenergylett.1c01678.

[36] J. Li, H. Zhang, W. Samarakoon, W. Shan, D.A. Cullen, S. Karakalos, M. Chen, D. Gu, K.L. More, G. Wang, Z. Feng, Z. Wang, G. Wu, Thermally driven structure and performance evolution of atomically dispersed FeN4 sites for oxygen reduction, Angew. Chem. 58 (52) (2019) 18971–18980, https://doi.org/10.1002/anie.201909312.

[37] Y.Y. Lin, K. Liu, K.J. Chen, Y. Xu, H.M. Li, J.H. Hu, Y.R. Lu, T.S. Chan, X.Q. Qiu, J.W. Fu, Tuning charge distribution of FeN4 via external N for enhanced oxygen reduction reaction, ACS Catal. 11 (10) (2021) 6304–6315, https://doi.org/10.1021/acscatal.0c04966.

[38] T. Najam, S.S.A. Shah, M.S. Javed, P.T. Chen, C.H. Chuang, A.L. Saad, Z.Q. Song, W. Liu, X.K. Cai, Modulating the electronic structure of zinc single atom catalyst by P/N coordination and Co2P supports for efficient oxygen reduction in Zn-Air battery, Chem. Eng. J. 440 (2022), 135928, https://doi.org/10.1016/j.cej.2022.135928.

[39] Q.L. Wang, C.Q. Xu, W. Liu, S.F. Hung, H.B. Yang, J. Gao, W. Cai, H.M. Chen, J. Li, B. Liu, Coordination engineering of iridium nanocluster bifunctional electrocatalyst for highly efficient and pH-universal overall water splitting, Nat. Commun. 11 (1) (2020) 4246, https://doi.org/10.1038/s41467-020-18064-w.

[40] G. Chen, Y. An, S. Liu, F. Sun, H. Qi, H. Wu, Y. He, P. Liu, R. Shi, J. Zhang, A. Kuc, U. Kaiser, T. Zhang, T. Heine, Q. Wu, X. Feng, Highly accessible and dense surface single metal FeN4 active sites for promoting the oxygen reduction reaction, Energ. Environ. Sci. 15 (6) (2022) 2619–2628, https://doi.org/10.1039/d2ee00542e.

[41] H. Yang, Y. Liu, Y. Luo, S. Lu, B. Su, J. Ma, Achieving high activity and selectivity of nitrogen reduction via Fe–N3 coordination on iron single-atom electrocatalysts at ambient conditions, ACS Sustain. Chem. Eng. 8 (34) (2020) 12809–12816, https://doi.org/10.1021/acssuschemeng.0c02701.

[42] L. Li, S. Huang, R. Cao, K. Yuan, C. Lu, B. Huang, X. Tang, T. Hu, X. Zhuang, Y. Chen, Optimizing microenvironment of asymmetric N,S-coordinated single-atom Fe via axial fifth coordination toward efficient oxygen electroreduction, Small 18 (2) (2021), e2105387, https://doi.org/10.1002/smll.202105387.

[43] T. Marshall-Roth, N.J. Libretto, A.T. Wrobel, K.J. Anderton, M.L. Pegis, N.D. Ricke, T.V. Voorhis, J.T. Miller, Y. Surendranath, A pyridinic Fe-N4 macrocycle models the active sites in Fe/N-doped carbon electrocatalysts, Nat. Commun. 11 (1) (2020) 5283, https://doi.org/10.1038/s41467-020-18969-6.

[44] R. Qin, K. Liu, Q. Wu, N. Zheng, Surface coordination chemistry of atomically dispersed metal catalysts, Chem. Rev. 120 (21) (2020) 11810–11899, https://doi.org/10.1021/acs.chemrev.0c00094.

[45] J. Xue, S. Deng, R. Wang, Y. Li, Efficient synergistic effect of trimetallic organic frameworks derived as bifunctional catalysis for the rechargeable zinc-air flow battery, Carbon 205 (2023) 422–434, https://doi.org/10.1016/j.carbon.2023.01.034.

[46] J. Zhang, Y. Zhao, C. Chen, Y.C. Huang, C.L. Dong, C.J. Chen, R.S. Liu, C. Wang, K. Yan, Y. Li, G. Wang, Tuning the coordination environment in single-atom catalysts to achieve highly efficient oxygen reduction reactions, J. Am. Chem. Soc. 141 (51) (2019) 20118–20126, https://doi.org/10.1021/jacs.9b09352.

[47] J. Joo, T. Kim, J. Lee, S.I. Choi, K. Lee, Morphology-controlled metal sulfides and phosphides for electrochemical water splitting, Adv. Mater. 31 (14) (2019), e1806682, https://doi.org/10.1002/adma.201806682.

[48] J. Gao, Y. Hu, Y. Wang, X. Lin, K. Hu, X. Lin, G. Xie, X. Liu, K.M. Reddy, Q. Yuan, H.J. Qiu, MOF structure engineering to synthesize CoNC catalyst with richer accessible active sites for enhanced oxygen reduction, Small 17 (49) (2021), e2104684, https://doi.org/10.1002/smll.202104684.

[49] T. Lu, X. Hu, J. He, R. Li, J. Gao, Q. Lv, Z. Yang, S. Cui, C. Huang, Aqueous/solid state Zn-air batteries based on N doped graphdiyne as efficient metal-free bifunctional catalyst, Nano Energy 85 (2021), 106024, https://doi.org/10.1016/j.nanoen.2021.106024.

[50] X. Wang, S. Ding, T. Yue, Y. Zhu, M. Fang, X. Li, G. Xiao, Y. Zhu, L. Dai, Universal domino reaction strategy for mass production of single-atom metal-nitrogen catalysts for boosting CO_2 electroreduction, Nano Energy 82 (2021), 105689, https://doi.org/10.1016/j.nanoen.2020.105689.

[51] L.T. Ma, S.M. Chen, Z.X. Pei, Y. Huang, G.J. Liang, F.N. Mo, Q. Yang, J. Su, Y.H. Gao, J.A. Zapien, Single-site active iron-based bifunctional oxygen catalyst for a compressible and rechargeable zinc-air battery, ACS Nano 12 (2) (2018) 1949–1958, https://doi.org/10.1021/acsnano.7b09064.

[52] T. Zhang, J. Bian, Y. Zhu, C. Sun, FeCo nanoparticles encapsulated in N-doped carbon nanotubes coupled with layered double (Co, Fe) hydroxide as an efficient bifunctional catalyst for rechargeable zinc-air batteries, Small 17 (44) (2021), e2103737, https://doi.org/10.1002/smll.202103737.

[53] J. Wang, H. Wu, D. Gao, S. Miao, G. Wang, X. Bao, High-density iron nanoparticles encapsulated within nitrogen-doped carbon nanoshell as efficient oxygen electrocatalyst for zinc-air battery, Nano Energy 13 (2015) 387–396, https://doi.org/10.1016/j.nanoen.2015.02.025.

[54] Y. He, H. Guo, S. Hwang, X. Yang, Z. He, J. Braaten, S. Karakalos, W. Shan, M. Wang, H. Zhou, Z. Feng, K.L. More, G. Wang, D. Su, D.A. Cullen, L. Fei, S. Litster, G. Wu, Single cobalt sites dispersed in hierarchically porous nanofiber networks for durable and high-power PGM-free cathodes in fuel cells, Adv. Mater. 32 (46) (2020), e2003577, https://doi.org/10.1002/adma.202003577.

[55] J.M. Chen, Y. Cheng, Q. Zhang, C. Luo, H.Y. Li, Y. Wu, H. Zhang, X. Wang, H. Liu, X. He, J. Han, D.L. Peng, M. Liu, M.S. Wang, Designing and understanding the superior potassium storage performance of nitrogen/phosphorus Co-doped hollow porous bowl-like carbon anodes, Adv. Funct. Mater. 31 (1) (2020), 2007158, https://doi.org/10.1002/adfm.202007158.

[56] I.S. Amiinu, X. Liu, Z. Pu, W. Li, Q. Li, J. Zhang, H. Tang, H. Zhang, S. Mu, From 3D ZIF nanocrystals to Co-Nx/C nanorod array electrocatalysts for ORR, OER, and Zn-Air batteries, Adv. Funct. Mater. 28 (5) (2018), 1704638, https://doi.org/10.1002/adfm.201704638.

[57] J. Sun, H. Xue, L. Lu, M. Gao, N. Guo, T. Song, H. Dong, J. Zhang, L. Wu, Q. Wang, Atomic-level modulation of local coordination environment at Fe single-atom sites for enhanced oxygen reduction, Appl. Catal. B: Environ. 313 (2022), 121429, https://doi.org/10.1016/j.apcatb.2022.121429.

[58] C. Shao, L. Wu, H. Zhang, Q. Jiang, X. Xu, Y. Wang, S. Zhuang, H. Chu, L. Sun, J. Ye, B. Li, X. Wang, A versatile approach to boost oxygen reduction of Fe-N4 sites by controllably incorporating sulfur functionality, Adv. Funct. Mater. 31 (25) (2021), 2100833, https://doi.org/10.1002/adfm.202100833.